

The Cosmic-Ray Experiment KASCADE

T. Antoni ^a, W.D. Apel ^b, F. Badea ^{a,1}, K. Bekk ^b, A. Bercuci ^{b,1},
H. Blümer ^{b,a}, H. Bozdog ^b, I.M. Brancus ^c, C. Büttner ^a,
A. Chilingarian ^d, K. Daumiller ^a, P. Doll ^b, J. Engler ^{b,2},
F. Feßler ^b, H.J. Gils ^b, R. Glasstetter ^a, R. Haeusler ^a,
A. Haungs ^b, D. Heck ^b, J.R. Hörandel ^a, A. Iwan ^{a,e},
K.-H. Kampert ^{a,b}, H.O. Klages ^b, G. Maier ^b, H.J. Mathes ^b,
H.J. Mayer ^b, J. Milke ^b, M. Müller ^b, R. Obenland ^b,
J. Oehlschläger ^b, S. Ostapchenko ^{a,3}, M. Petcu ^c, H. Rebel ^b,
M. Risse ^b, M. Roth ^a, G. Schatz ^b, H. Schieler ^b, J. Scholz ^b,
T. Thouw ^b, H. Ulrich ^b, A. Vardanyan ^d, J. Weber ^b, A. Weindl ^b,
J. Wentz ^b, J. Wochele ^b, J. Zabierowski ^e, and S. Zagromski ^b
(KASCADE-Collaboration)

^a*Institut für Experimentelle Kernphysik, Universität Karlsruhe, 76021 Karlsruhe, Germany*

^b*Institut für Kernphysik, Forschungszentrum Karlsruhe, 76021 Karlsruhe, Germany*

^c*National Institute of Physics and Nuclear Engineering, 7690 Bucharest, Romania*

^d*Cosmic Ray Division, Yerevan Physics Institute, Yerevan 36, Armenia*

^e*Soltan Institute for Nuclear Studies, 90950 Lodz, Poland*

Abstract

KASCADE has been designed to measure air showers of primary cosmic-ray energies in the PeV region and to investigate the *knee* phenomenon in the all-particle energy spectrum. Several observables are measured simultaneously for each event by different detector systems. The experiment started to take data in 1996 and has been completed and extended since then. The individual detector systems and their performances are described. Also, the experience in long-term operation of the experiment and the interplay between different components is outlined.

1 Introduction

¹ on leave of absence from ^c

² corresponding author, e-mail: engler@ik.fzk.de

³ on leave of absence from Moscow State University 119899 Moscow, Russia

Investigating cosmic rays of primary energies around 1 PeV and above is presently

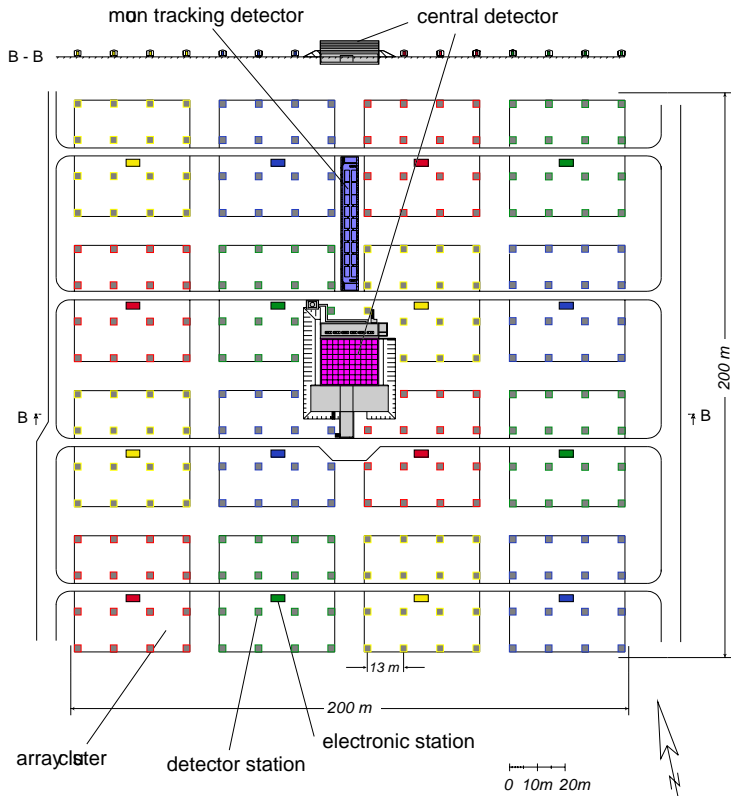


Fig. 1. Schematic layout of the KASCADE experiment.

possible only with ground-based detector systems. With these installations large surface areas and long exposure times can be realized to cope with the low particle flux at high energies. Measurements above the atmosphere using detector systems on satellites, spacecrafts, or balloons are limited in acceptance area and observation time and run out of statistics at about 1 PeV primary energy.

For ground-based experiments astrophysically relevant parameters like energy, mass, or direction of incoming cosmic-ray particles have to be deduced from the particle distributions in the extensive air showers (EAS) which they initiate in the atmosphere. Therefore, as many different observables as possible have to be measured simultaneously from which the properties of the primaries have to be calculated. Also, a thorough check of the interaction model

used when simulating the EAS is important because the physics of the hadronic interaction at the high energies in question and in the very forward direction has been investigated at accelerators only scarcely and, thereby, is not known sufficiently well.

The experiment KASCADE (**KA**rlsruhe **S**hower **C**ore and **A**rray **D**Etector) has been conceived following these aspects [1]. It is placed at the laboratory site of the Forschungszentrum Karlsruhe in the Rhine valley at 110 m a.s.l. (49° n, 8° e) and takes data continuously since 1996. In the present article an overall description of the experimental performance is given including the interplay of a multi-component installation, its resolutions, and long-term stability.

Table 1

Detector components of KASCADE, their total sensitive area and threshold for vertical particles.

Detector	Particle	Total area [m ²]	Threshold
array, liquid scintillators	e/ γ	490	5 MeV
array, plastic scintillators	μ	622	230 MeV
muon tracking detector, streamer tubes	μ	128 \times 4 layers	800 MeV
central detector:			
calorimeter, liquid ionization chambers	h	304 \times 8 layers	50 GeV
trigger layer, plastic scintillators	μ	208	490 MeV
top cluster, plastic scintillators	e/ γ	23	5 MeV
top layer, liquid ionization chambers	e/ γ	304	5 MeV
multi-wire proportional chambers	μ	129 \times 2 layers	2.4 GeV
limited streamer tubes	μ	250	2.4 GeV

2 Experimental set-up

The experiment measures the electromagnetic component with an array of scintillation counters, the muonic component by scintillators and tracking chambers at four different energy thresholds and the hadronic component in a sampling calorimeter. Figure 1 shows the schematic layout with the three main components: detector array, central detector and muon tracking detector on a surface of 200×200 m². Figure 2 gives an idea of the particle intensities in a typical EAS of 1 PeV primary proton and their dependence on the projected distance to the shower core as obtained with the EAS simulation program CORSIKA [2]. The electromagnetic component comprises by far the highest particle densities whereas energetic hadrons can be found in an appreciable number only near the shower core. One also observes that the number of electrons, which comprises also positrons and gammas exceeds the number of muons near the centre by nearly three orders of magnitude. This and the presence of hadrons make the detection of muons near the shower axis an experimental challenge.

The different detector components which

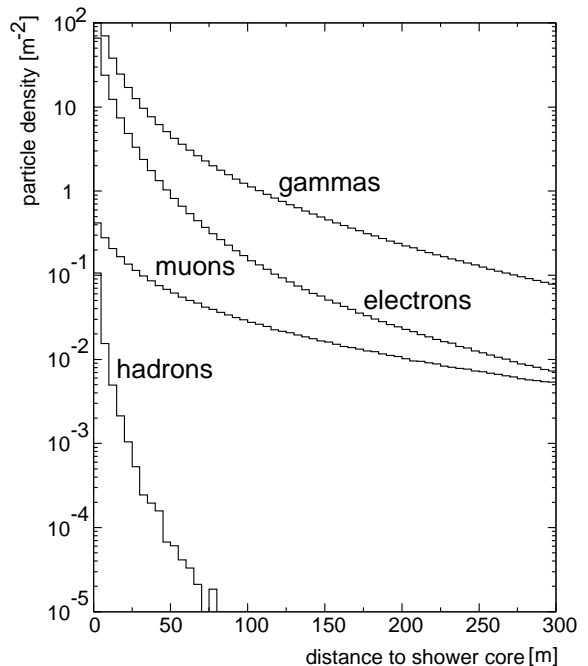


Fig. 2. Simulated particle densities vs. distance to the shower core for an average EAS initiated by a 1 PeV proton at sea level and a zenith angle of 22° . Thresholds are 5 MeV for gammas and electrons, 230 MeV for muons, and 50 GeV for hadrons.

are described in the following are compiled in Table 1. Given are the total detector area and the threshold for vertical particles.

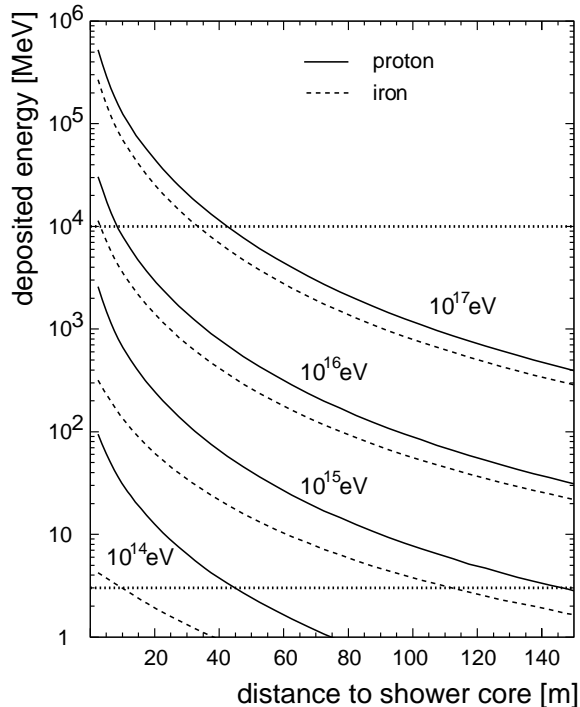


Fig. 3. Energy deposited in an unshielded scintillation detector for different energies of primary protons as well as iron nuclei and zenith angle of 22° vs. core distance. The horizontal lines border the signal domain required to measure showers of 10^{14} up to 10^{17} eV primary protons.

3 Detector array

The scintillation detectors of the array are housed in 252 stations on a grid with 13 m spacing and are electronically organized in clusters of 16 stations, the inner clusters only with 15 stations, see Figure 1. In order to optimize the layout, the shower particles generated with CORSIKA have been tracked through the detector simulation code CRES, which is based on the GEANT3 code [3]. It generates the same signal response as the real detectors do. As result, a detector coverage of 1.3% for the electromagnetic and 1.5% for the muonic component has been chosen. With this level of electron sampling the accuracy in

EAS reconstruction is dominated by the intrinsic shower fluctuations and not by the sampling statistics. In order to determine the required dynamic range of the electron counters, the energy deposited in the scintillators has been simulated for different primary energies. The outcome is shown in Figure 3. It necessitates a dynamic range of at least 1:3000 if showers of primary energies from 100 TeV up to 100 PeV are to be detected.

3.1 Detector station

A profile view of a detector station is presented in Figure 4. Four e/γ detectors are positioned on a lead/iron plate (10 cm Pb and 4 cm Fe), and entailing a 230 MeV threshold for vertical muons in the segmented muon detector below the absorber. In fact, two types of detector stations exist. The four inner clusters have no muon detectors installed since close to the shower core the punch-through of the electromagnetic and the hadronic component makes them redundant for central showers. On the other hand, the twelve outer clusters contain only two e/γ detectors per station.

3.2 e/γ detector

When designing the e/γ detector the following criteria were carefully considered [4], especially

- time resolution < 1 ns
- energy resolution $< 10\%$ for muons
- dynamic range $\approx 1 : 8000$
- temperature range -20° to 40° C
- low cost

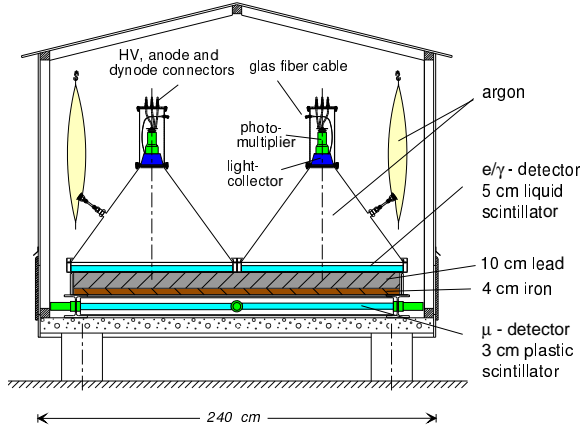


Fig. 4. Sketch of a fully equipped array station with four e/γ detectors on top of a Pb/Fe absorber plate and a segmented muon detector.

These requirements led to a liquid scintillator filled in a circular tub of 1 m diameter and 5 cm height with a light collection cone in vertical direction as sketched in Figure 4. For the scintillator 25 different organic plastic and liquid materials have been tested and the final choice was the PDP liquid scintillator. This liquid with 2 g/l of scintillator PMP (1-phenyl-3-mesityl-2-pyrazoline) in 80% (volume) paraffin and 20% pseudocumene has been worked out on site and proved to fulfill the requirements, i.e. scintillating decay time of 2.5 ns, good transparency, and working also at low temperatures. Light collection by diffusive reflection through a white paint (Panit) in the circular tub and on the light collection cone proved to be very efficient. In addition, a light collector of lucite in front of the photomultiplier enhances the signal by an extra factor of 1.8.

As photomultipliers the 3" diameter EMI 9822 and Valvo XP3462 were chosen. To deal with the required dynamic range, signals are picked up from the anode and from one of the dynodes. The energy resolution of the detector has been measured to about 8% at 12 MeV, the mean energy deposit of a minimum ionizing particle (m.i.p.). The

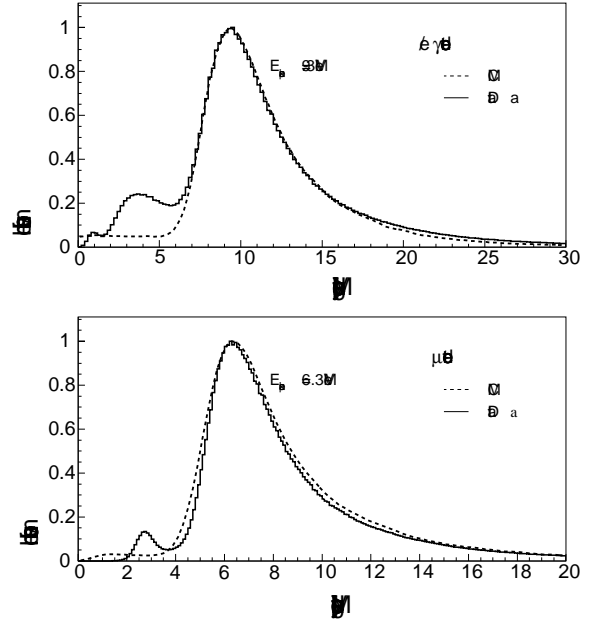


Fig. 5. Average energy deposit for single muon trigger in the e/γ -detectors (upper graph) and the μ detectors (lower graph). The dashed lines represent Monte Carlo simulation taking the angle and momentum distribution of muons into account.

time resolution of the detector for passing muons has been determined to $\sigma = 0.77$ ns. Energy deposits equivalent to 2000 m.i.p. can be detected linearly with a threshold of 1/4 m.i.p. which corresponds approximately to 3 MeV. During data taking the energy calibration is checked repeatedly by self-triggering the counters on single muons and accumulating spectra as shown in the upper graph of Figure 5. The dashed lines represent the expected energy deposit of single cosmic-ray muons taking their angle and momentum distribution into account.

3.3 Muon detector

The layout of a muon detector placed below the shielding is shown in Figure 6. It consists of four 3 cm thick plastic scintillators of the type Bicron BD-416 (90×90 cm²).

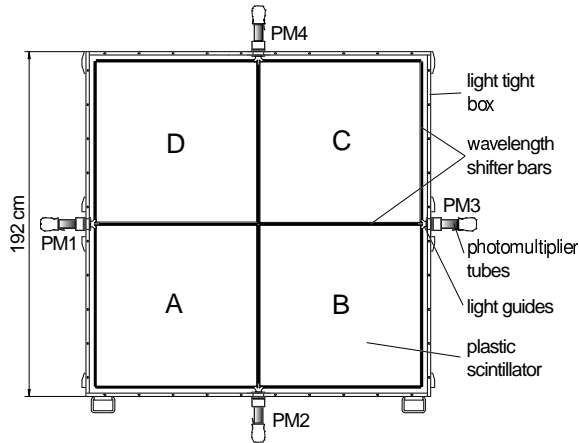


Fig. 6. Sketch of a muon detector in an array detector station.

The light is coupled out on all four sides by wavelength shifter bars and transferred via lucite light guides to four 1.5" photomultipliers (type EMI 9902 or Valvo XP2081) using silicon pillows for the connection. The read-out of the scintillators by two photomultipliers using the wavelength shifter technique yields a very good spatial uniformity [5]. Tests revealed that the sum signal shows a spatial non-uniformity of $\sigma = 2\%$ only. The energy resolution of the detector has been determined to about 10% at 8 MeV, the mean energy deposit of a m.i.p., and the time resolution to $\sigma = 2.9$ ns.

The method of read-out, however, implies an optical cross-talk between neighbouring scintillator slabs. The amount of this cross-talk was investigated by measuring, e.g. the response of PM3 for signals in scintillator A (sum of PM1 and PM2). A medium value of contamination of the true signal by cross-talk was found to be of the order of 10%.

3.4 Data acquisition

The data acquisition, trigger, and the detector control in the array is organized on the cluster level, so that each cluster acts as

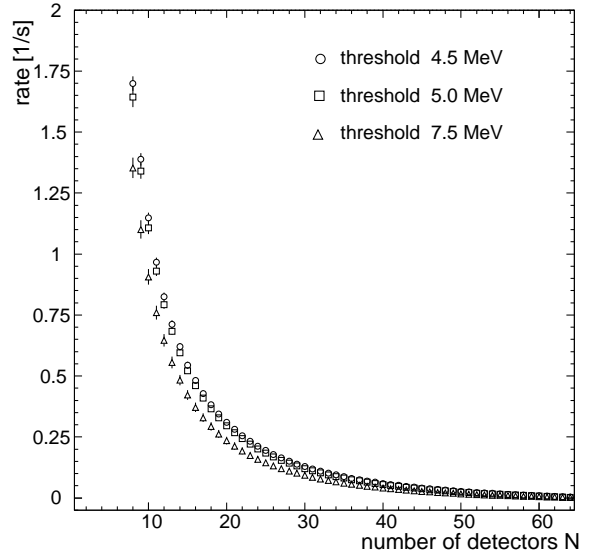


Fig. 7. Trigger rate in a cluster vs. multiplicity of e/γ detector hits ($N/64$).

an independent experimental component [6]. The corresponding VME-based front-end electronics and processors are installed inside the electronic stations (see Figure 1), which also contain the HV control, a clock module, and a trigger unit. The crates are controlled by TVC (**T**ransputer-based **V**ME **C**ontroller) modules. The front-end electronics consists of 8 KAFE modules (**K**ASCADE **A**rray **F**rontend **E**lectronics) for signal processing from all of the 16 stations. All signal and high-voltage cables are of equal length and run to the detector stations in tubes underground.

To correlate the data from different clusters and from all other components within the experiment, common clock signals are used. They are derived from a central GPS receiver and a rubidium high frequency generator. Synchronized pulse trails of 5 MHz and 1 Hz are distributed via fiber optic cables to the electronic stations. They are used to determine the trigger time (time label [200ns] and UTC time [1s]) and to assign time labels to each stored event.

On the KAFE modules all detector signals above discriminator thresholds are converted and stored temporarily in hardware FIFO memories (56 event blocks depth) including the time label. These data are read out from the 16 FIFOs and stored locally in a 1 MB software FIFO memory of the TVC in a continuous polling procedure. At the same time, these signals pass through pulse shapers and are sent to the trigger unit.

The determination of an event is performed by the trigger electronics [7], which generates a shower trigger, when a certain preset multiplicity condition in the cluster is fulfilled. These trigger signals are distributed via fiber optic cables to all parts of the experiment. The trigger rate of a cluster with a full set of 64 e/γ -detectors was measured as a function of the number of e/γ -detectors above a certain threshold. The result is shown in Figure 7. It does not depend significantly on the threshold used as long as the latter is below the one particle peak. However, it strongly depends on the multiplicity of coincidences. The envisaged trigger threshold of about 0.5 PeV for iron initiated showers necessitates a minimum multiplicity of $n_i = 20$ out of 60 for the inner and $n_o = 10$ out of 32 for the outer clusters, resulting in an overall rate of 3 events/s from the whole array.

When a trigger signal has been generated, the software FIFO memories in all cluster front-end electronics modules are searched for data with corresponding time labels (time difference less than $8 \mu s$). Then, the selected data are sent through the transputer array and a following transputer-link/ethernet gateway (B300) to the central workstation. In addition, a single muon trigger condition is used in each cluster to acquire local on-line control and calibra-

tion spectra.

On the workstation, the eventbuilder of the array is realized as a client server network. A server program is connected to the local hardware and software of the array and is the interface between the 16 clusters and the clients. The main tasks of the server are routing of data and control tags as well as building of events. Different types of clients are running on the central workstation. The control and display X11 Motif application (GUI) provides the user with shower data, pulse height as well as arrival time spectra, event statistics, an on-line and off-line 2D/3D eventdisplay, and is able to change hardware settings. Another client is the central eventbuilder, see chapter 6.

To measure the energy deposit per station, the photomultiplier signals of the corresponding e/γ detectors are integrated within 200 ns and digitized by three 8 bit ADCs. These ADCs are shifted against each other by approximately 4 bit to cope with the required dynamic range. The first ADC analyses an amplified anode signal, the second the anode, and the third a dynode. In this way the e/γ ADCs cover a signal range of about 1:5000 (1/4 to 1250 m.i.p.). This range can be extended by changing the overlap between the anode and dynode ADCs to less than 4 bit by a software preset. The threshold is set to 1/4 of a m.i.p. As for the muon detectors two ADCs are used only and the dynamic range is limited to about 1:240 (1/4 to 60 m.i.p.).

In addition, the event data block of each station contains the arrival time of the first particle in each of the two detector components per station. The resolution of the TDCs is about 270 ps. The time calibration is performed on-line on an event by

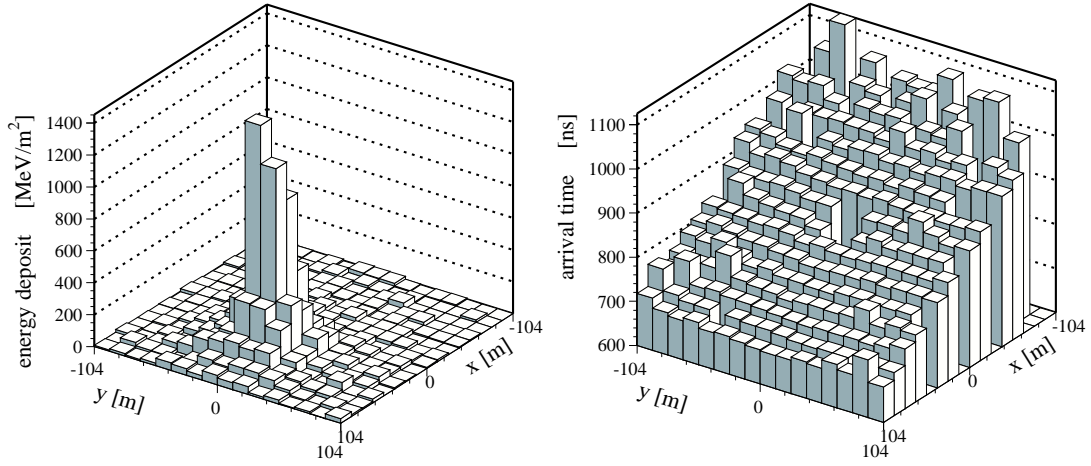


Fig. 8. Example of an EAS registered in the e/γ detectors: energy deposits (left) and arrival time (right). Reconstructed total number of electrons $N_e = 2.6 \cdot 10^5$.

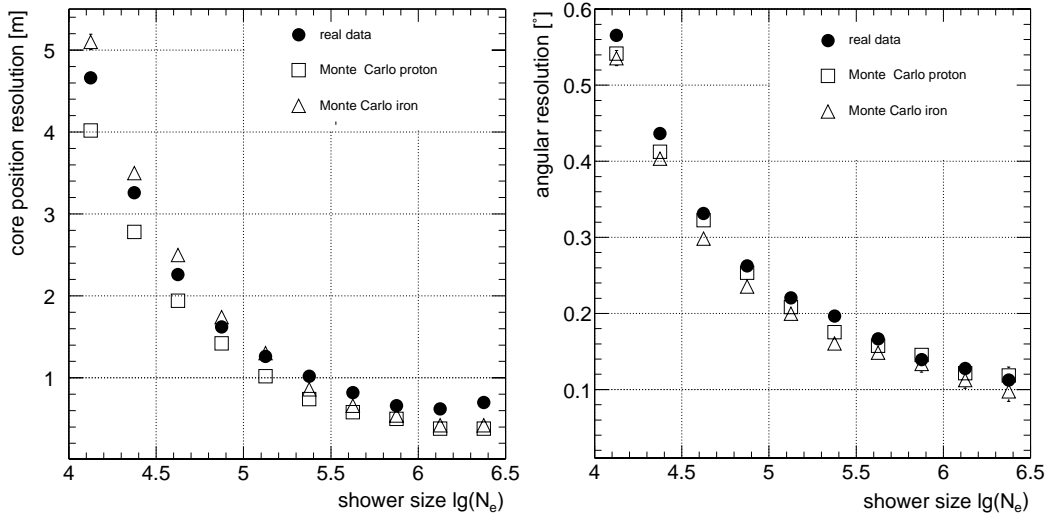


Fig. 9. Resolution of reconstructed shower core position and angle of incidence for simulated EAS of primary protons and iron nuclei (open symbols) versus the electron number N_e . The filled circles show the difference in reconstruction of shower core and incident angle by chequer board analyses of real data.

event basis. For this purpose, the detector signal starts the TDC and the stop signal is given by the first following edge of the 5 MHz clock. In parallel, a second measurement starts with the same signal but is stopped by the second following edge of the 5 MHz clock. The time difference of both TDC measurements has to be 200 ns. If the time interval to the first edge is less than 100 ns, the next clock edges (200 ns later) are used as stop and a corresponding flag is

set. This procedure is performed for both detector components per station.

Figure 8 shows, as an example, the energy deposits and arrival times of a particular event. The reconstructed electron number of $N_e = 2.6 \cdot 10^5$ corresponds approximately to a primary proton of 2 PeV. The number of electrons is calculated from the measured energy deposits by applying the on-line calibration with single muons (see Figure 5).

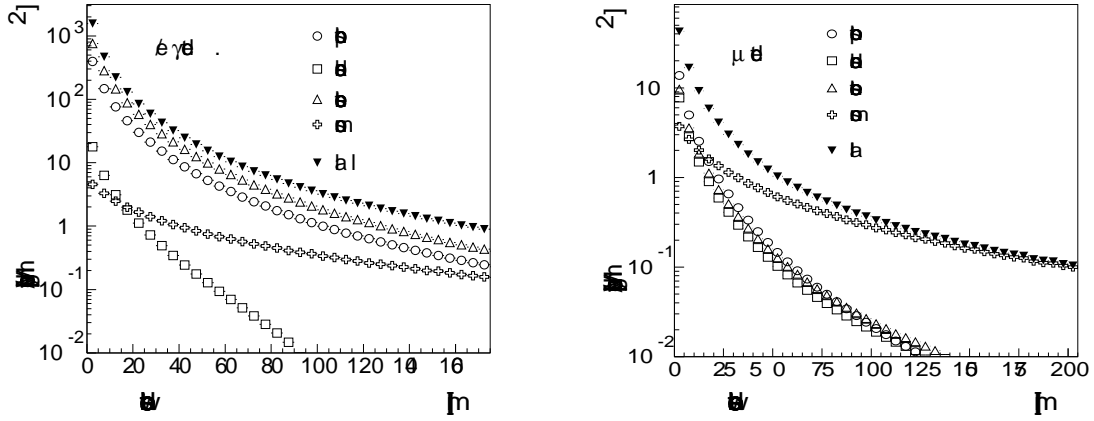


Fig. 10. Energy deposits in the e/γ (left graph) and μ detectors (right graph) for showers of primary protons of 1 PeV energy. The contributions of different components vs. shower core distance according to CORSIKA/CRES simulations are shown.

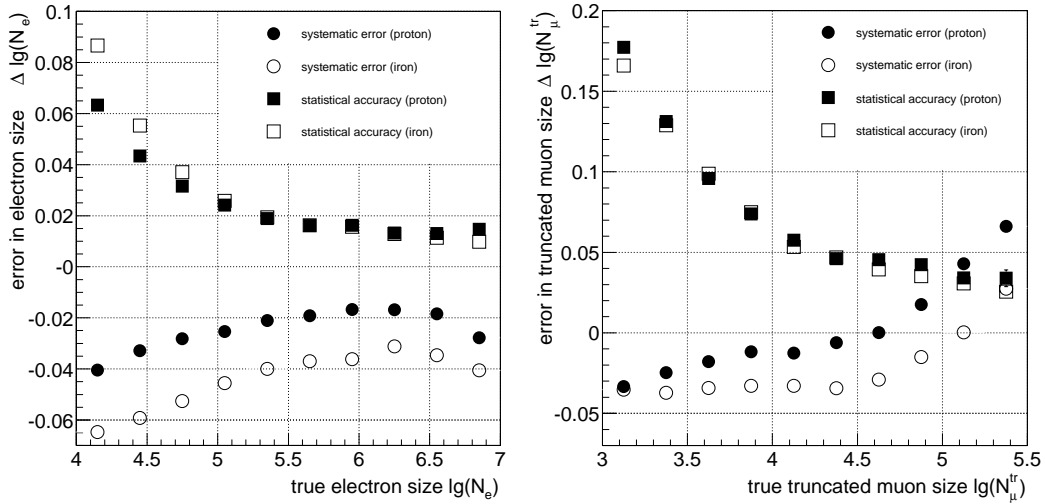


Fig. 11. The average difference (systematic error) and rms-width (statistical accuracy) of reconstructed $\log_{10} N_e$ (left graph) and $\log_{10} N_{\mu}^{tr}$ (right graph) versus particle numbers for EAS simulated with CORSIKA/CRES. Filled symbols represent primary protons and open symbols primary iron nuclei.

Details are given elsewhere [8].

The performance of the local DAQ software running on the cluster transputers is characterized by 1 μ s interrupt latency, 30 μ s dead time after showers and $\simeq 7$ ms total time to process a shower event. The total uncorrelated event rate in a cluster is 2 to $3 \cdot 10^4$ /s.

In one of the outer clusters the arrival times are measured using a FADC system (type

DL 515, Struck company). By these units the hits of arriving particles at the same detector are registered with a sampling rate of 1 GHz and the time structure of the particle disk in an EAS is studied. In particular, delayed particles can be looked for up to 1 μ s behind the shower front.

3.5 Reconstruction of shower parameters

In a first step fast algorithms are used to roughly estimate the shower parameters. To obtain a quick indication of the core position a neural network has been developed [9]. The shower direction is calculated by a gradient method from the arrival times [10]. Taking these values as starting points the final parameters are calculated in fitting procedures using empirical functions for lateral particle distributions and the shower front shape.

Figure 9 shows the accuracy attained by a final fit for data from CORSIKA/CRES simulations (open symbols). The accuracy is estimated applying a chequer board analysis, i.e. one uses only every second detector and compares the parameter obtained from the two data sets. The findings are presented in the graphs, corrected for the effect of smaller statistics. Light and heavy primaries do not differ markedly and we can check the results with real data which are a mixture of primary masses (filled circles). One can state that they compare well with the estimations using simulated showers.

When reconstructing the electron number N_e and muon number, one has to consider that all components of an air shower contribute to the energy deposits in the detectors, see Figure 2. In order to take these effects into account, air shower events were simulated with the CORSIKA generator and all particles at observation level passed through the CRES code. Figure 10 shows an example of expected energy deposits of different types of particles in the e/γ and muon detectors as a function of the distance from the shower core for a 1 PeV primary proton and zenith angle $\Theta = 22^\circ$. One observes that the very abundant pho-

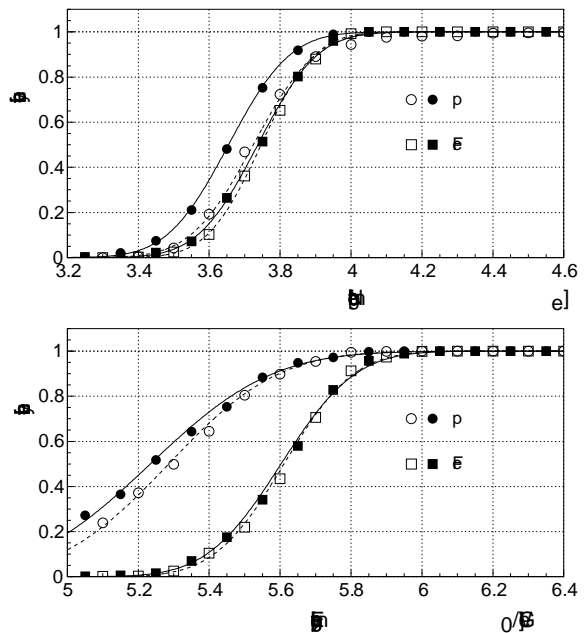


Fig. 12. Trigger efficiency (filled symbols), combined with reconstruction efficiency (open symbols) for simulated proton and iron induced showers versus electron size (upper graph) and primary energy (lower graph). CORSIKA/CRES simulation for trigger condition $n_i = 20$, $n_o = 10$, see text.

tions and electrons deposit a large amount of energy in the e/γ detector whilst hadrons and muons contribute only small amounts close to the shower axis. In contrast, at distances far from the shower core the energy deposit caused by muons becomes similar to that of electrons and photons. The lateral distributions are assumed to follow a NKG form with a Molière radius of 89 m for electrons and 420 m for muons. Details are discussed elsewhere [8]. In the muon detectors, as can be seen in the right graph of Figure 10, a significant punch-through of electrons, photons, and hadrons exists close to the core. Therefore, as muon number the truncated muon size N_μ^{tr} is calculated by integrating between 40 m and 200 m only.

To correct for the effect of energy deposit of muons in the e/γ detectors and the punch-through in muon detectors, a large set of

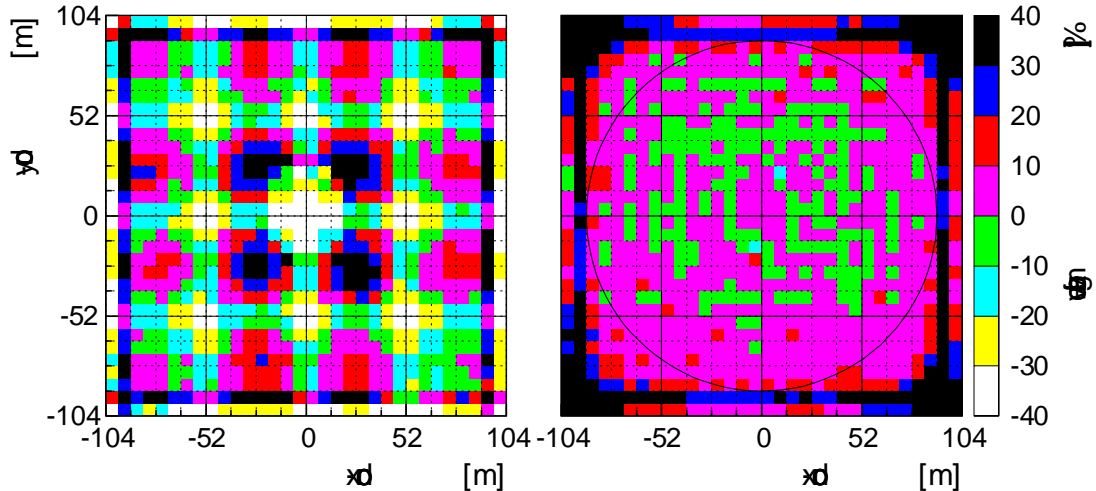


Fig. 13. Frequency distribution of reconstructed core positions for triggered EAS ($n_i = 20$, $n_o = 10$). Left graph: all electron sizes N_e , right graph: $N_e > 30000$. The average number of entries per cell are 69000 for the left and 6500 for the right graph.

proton and iron induced showers for different energies and angles was generated. From these MC simulations lateral energy correction functions were calculated which allow to obtain the number of electrons and muons from the energy deposits in the respective counters. It turned out that these functions depend only weakly on the energy, mass, and angle of the primary particle, thus averaged functions can be used.

The accuracy in reconstruction of the particle numbers, viz. the electron and muon size, N_e and N_μ^{tr} respectively, is presented in Figure 11 for primary protons and iron nuclei. The two graphs represent the results after three iterations in the fitting procedure. Plotted are the mean differences of the logarithms of reconstructed particle numbers versus the CORSIKA size. The circles show that small systematic errors exist which depend among others on the interaction codes used and are corrected for in the analysis procedures. The squares represent the statistical accuracy, i.e. the rms-width of the corresponding distributions. In case of N_e one observes that the statistical accuracy improves from 18% at

$\log_{10} N_e = 4.1$ (approximately at the trigger threshold) to about 4% at $\log_{10} N_e = 6.0$ which corresponds to about 5 PeV for primary protons.

The trigger efficiency as obtained from simulated EAS is plotted in Figure 12 for primary proton and iron showers. As mentioned above, the trigger condition requires that $n_o = 10$ e/γ detectors have a signal over threshold in an outer cluster or $n_i = 20$ in an inner cluster. The upper graph shows the efficiency with respect to the true electron number. One notices that for $N_e \approx 15000$ the trigger efficiency attains nearly 100% and that the electron distribution of light and heavy primaries have only minor influence on the trigger. In the lower graph the efficiency is plotted versus the primary energy and the difference between p and Fe becomes apparent. Also, the reconstruction efficiency is given. In case of heavy primaries nearly all triggered EAS can be reconstructed, whereas for primary protons a steeper electron lateral distribution accounts for some reconstruction inefficiencies at small energies.

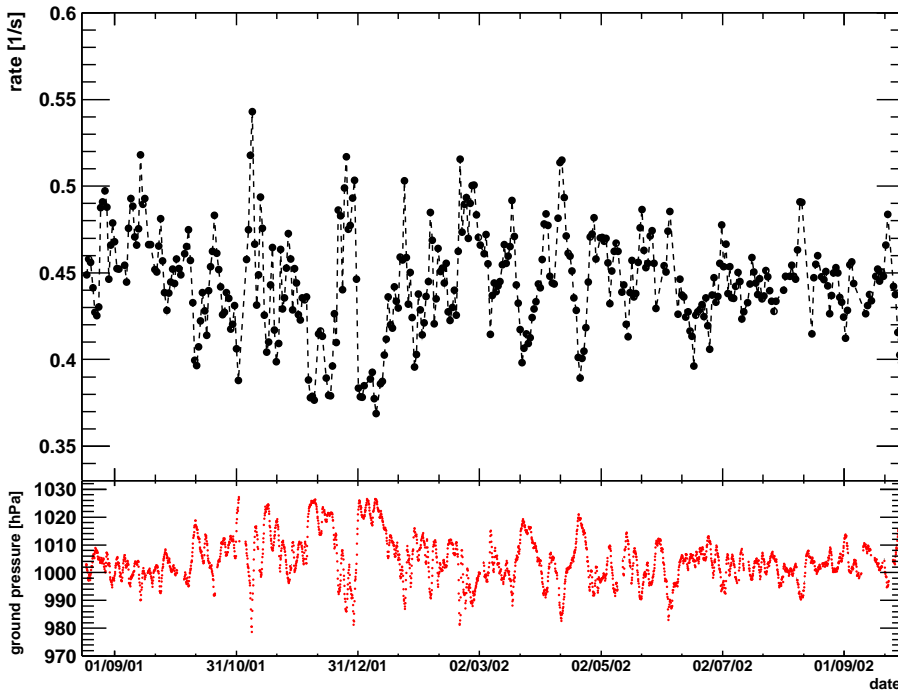


Fig. 14. Average shower rate versus time for EAS with $N_e > 10^4$ (upper graph). Barometric pressure at the laboratory site for the same time period (lower graph).

Figure 13 shows the frequency distribution of reconstructed core positions as a scatter plot on the array surface. At threshold the trigger condition causes the cluster structure to appear, but for $N_e > 30000$, i.e. an EAS of about 0.5 PeV primary proton, the trigger efficiency becomes uniform. In order to avoid edge effects in most analyses only EAS with their cores within a radius of 91 m are accepted.

The average rate of showers versus time for one year of operation is shown in Figure 14. Plotted is the number of EAS with an electron size $N_e > 10^4$. The fluctuations are strongly correlated with the atmospheric ground pressure, as can be noticed by comparing the barometric pressure given in the lower graph for the same time period.

4 Central detector

A sketch of the central detector with an area of 320 m² is displayed in Figure 15. It consists of a hadron sampling calorimeter with 8 tiers of iron absorber interspersed with 9 layers of warm-liquid ionization chambers. Below the third absorber plane a layer of plastic scintillators serves as detector for studies of the EAS time structure and to trigger the read-out of the ionization chambers as well as the muon detectors in addition to the array trigger. The multi-wire proportional chambers together with a layer of limited streamer tubes are located in the basement below the iron absorber and measure high-energy muons by tracking. On top of the installation, above the lead filter, the first layer of liquid ionization chambers and a cluster of

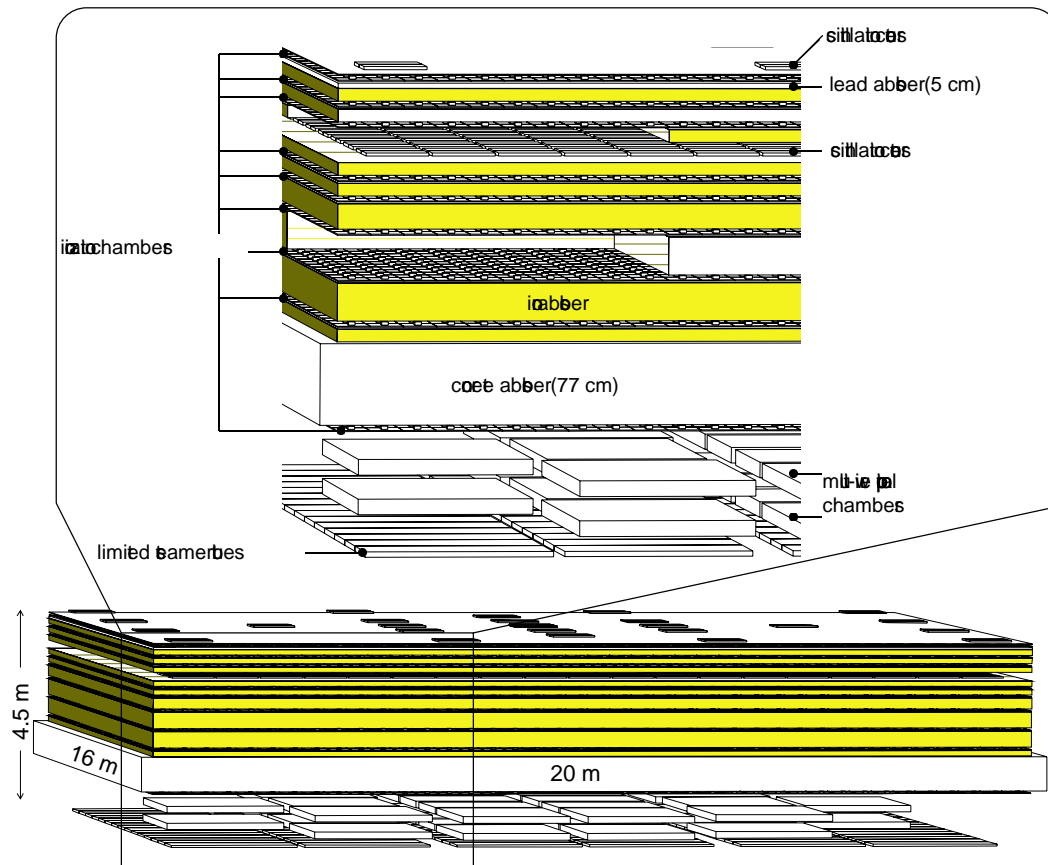


Fig. 15. Schematic lay-out of the central detector. General view (lower graph) and partly exploded view (upper graph). The hadron calorimeter consists of 9 tiers of lead, iron, and concrete absorbers interspersed with 9 layers of warm-liquid ionization chambers. The third gap houses a layer of plastic scintillators for trigger purposes. In the basement below the concrete ceiling two layers of multi-wire proportional chambers and one layer of limited streamer tubes for muon tracking are installed. On the top a cluster of plastic scintillation counters is placed.

scintillators are used to investigate thoroughly the electromagnetic cores of EAS and small showers.

4.1 Hadron calorimeter

The main part of the central detector is the finely segmented calorimeter with a total of about 11 000 chambers and 44 000 read-out channels. A description of the calorimeter and first results can be found in [11].

The ionization chambers are filled with purified tetramethylsilane (TMS) or tetra-

methylpentane (TMP). One of the principal motivations to use liquid ionization chambers in a cosmic-ray experiment is their long-term stability and the high dynamic range. The electronic feedback amplifier chain fulfills these requirements. For the actual chamber signal the time stability is proven by the stable rate as documented in Figure 16. The diagram shows the average rate of single hadrons with an energy above the indicated threshold. The flux of cosmic-ray hadrons is known to be very stable and the energy spectrum is a steeply falling power law, hence, a constant rate sensitively reflects the signal stability. The

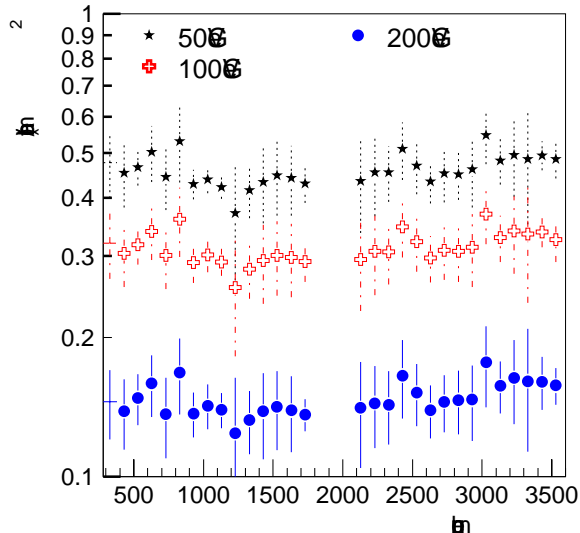


Fig. 16. Average hadron rate in the calorimeter per monthly time interval vs. run number representing a period of five years. The different symbols represent the indicated energy thresholds for hadron detection.

horizontal scale in Figure 16 corresponds to five years of operation, the first chambers had been filled already 10 years ago. The gap around run number 2000 emerged during the installation of the top layer (see section 4.4) when the high voltage on the chambers had to be switched off.

The thickness of the calorimeter corresponds to 11.5 nuclear interaction lengths in vertical direction, so that hadrons up to 25 TeV are absorbed with less than 2.5% energy leakage. The dynamic range of the electronics is about $1 : 6 \cdot 10^4$. This allows to read out the signal of one passing muon (0.8 MeV) up to 12 GeV of deposited energy in an individual channel in a shower core without saturation.

The detector is controlled and monitored via a transputer based parallel computer on which a multi-user operating system is installed. The parallel computer hosts also a local event builder which merges the data blocks from the different sub-units on

the basis of time labels contained in each sub-event. The system is controlled locally via a PC or remotely via a user server installed on the central workstation. The latter allows the connection of graphical user interfaces and passes event data to connected processes, like the central event builder or event displays. The detector status, its performance, and stability are automatically supervised every 30 min by a process on a workstation, also connected to the calorimeter via the user interface. In case of faulty conditions scientists on duty are alarmed.

Two examples of hadronic events in the calorimeter are shown in Figure 17. The left graph shows a single hadron reconstructed with a total energy of 12 TeV. The figure illustrates the low noise level of the detector. The right side depicts a shower core with 28 reconstructed hadrons with a total energy of $\sum E_h = 15.8$ TeV, originating from a primary particle of about 4 PeV. Each pixel represents the energy collected on an electrode with pad size of 25×25 cm².

To manage these different types of events, two reconstruction codes have been developed: One for single or well separated, individual hadrons which optimizes the reconstruction of shower axis and total energy, as described in [11]. Typically, for a 1 TeV hadron an energy resolution with a rms-value of 20% and an angular resolution of 3° is achieved. A second code is used for analyzing hadronic shower cores and traces out as many hadrons as possible, as well as their energies and axes. It is explained in detail elsewhere [8]. Typically, two hadrons of nearly equal energy are resolved with 50% probability if their axes are separated by 40 cm [12].

The reconstruction ability for hadronic

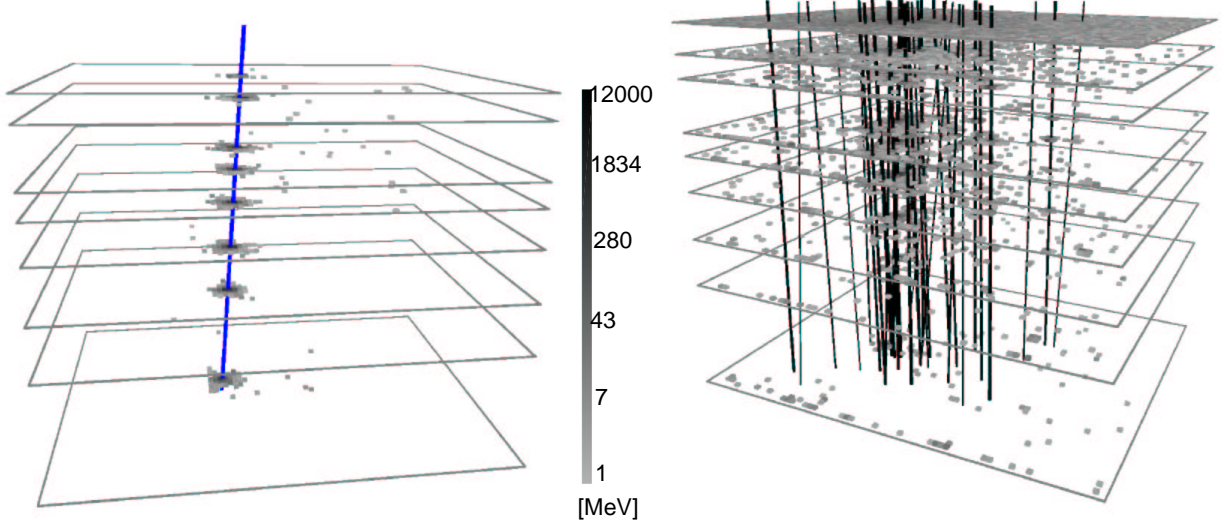


Fig. 17. Pattern of two hadronic events in the calorimeter. Each pixel represents the deposited energy on a pad of $25 \times 25 \text{ cm}^2$. The straight lines represent the reconstructed hadron axes. Left: single hadron event, reconstructed energy 12 TeV. Right: shower core with 28 reconstructed hadrons and an energy sum of $\sum E_h = 15.8 \text{ TeV}$.

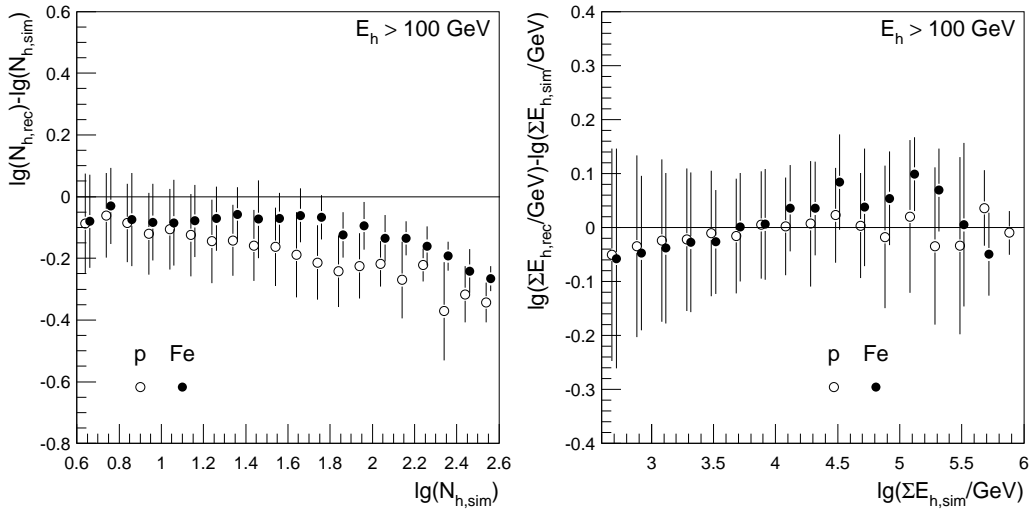


Fig. 18. The relative difference of reconstructed to simulated number of hadrons in shower cores versus the simulated number (left panel). Relative difference in reconstructed to simulated hadronic energy sum versus the simulated energy sum (right panel). CORSIKA calculations for primary protons and iron nuclei. The error bars represent the rms-values of the distribution.

cores is presented in Figure 18. Showers of primary energy 0.5 - 50 PeV have been simulated with the CORSIKA code, their cores falling in the middle of the calorimeter. The left graph shows the relative difference in the number of reconstructed to simulated hadrons. One observes that for

large hadron numbers not all cascades can be recovered in the analysis. As an example, in the mean, out of 100 infalling hadrons more than 80 are reconstructed. The losses of hadrons occur in the very centre, where the hadron density is high and individual hadrons cannot be resolved

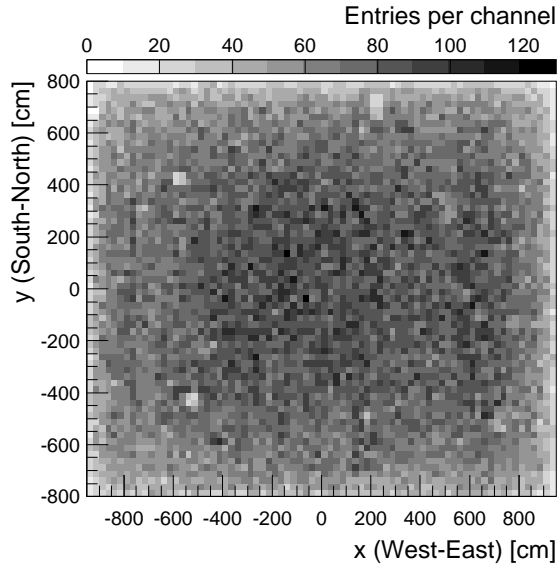


Fig. 19. Frequency of hits on the calorimeter surface for reconstructed hadrons.

due to the overlap of their cascades. For primary iron nuclei the hadrons in an EAS core are less concentrated so that a higher percentage can be resolved. The total energy, however, is well reconstructed as can be seen in the right graph of Figure 18. Up to 1 PeV of hadronic energy can be measured in the calorimeter to within 15% accuracy. The surplus found in dense and high-energy cores is of electromagnetic and muonic origin and also consists of low energy hadrons. It is corrected for in the analysis procedures.

The spatial uniformity of hadron detection is demonstrated by means of the scatter plot in Figure 19. The graph shows the distribution of all reconstructed hadrons ($E \geq 50$ GeV) for shower cores falling onto the calorimeter surface. The data represent $3.6 \cdot 10^4$ showers taken in a time period of 12 months. The lower population at the edges is caused by the particular selection of EAS in the analysis and is also present in the corresponding simulations. The few small areas of reduced response are caused by malfunctioning amplifier channels, but repre-

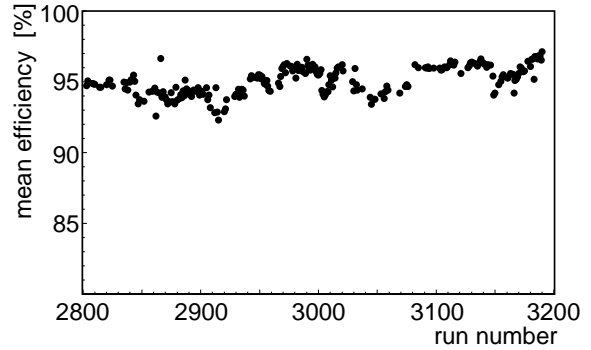


Fig. 20. Mean efficiency of the multi-wire proportional chambers for individual runs for one year of operation.

sent less than 1% of the active calorimeter surface.

4.2 Muon chamber system

For vertical muons the absorber of the calorimeter sets a threshold of 2.4 GeV. Positions and angles for these energetic muons are measured by two layers of multi-wire proportional chambers (MWPC) below the absorber in the basement, for the arrangement see Figure 15. A detailed description of the chamber system and operational tests can be found in [13]. As counting gas Ar/CH₄ is used. The anode wires and the inclined cathode strips on both sides are read out and determine the muon position with a precision of $\sigma = 1.1$ cm. The distance between the two layers of chambers is 38 cm. This translates to an angle accuracy of $\sigma = 1.5^\circ$. Tracks can be classified as muons belonging to the particular EAS if their inclinations agree well with the shower direction within this angular uncertainty.

Figure 20 shows as an example of long-term reliability the mean efficiency for track reconstruction versus the run number for one year of detection time.

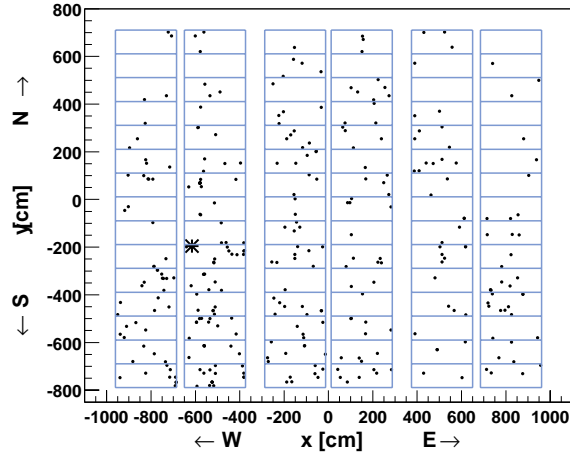


Fig. 21. Example of hit distribution in the streamer tube layer for an EAS with $\log_{10} N_{\mu}^{tr} = 3.9$ corresponding to a primary energy of about 2.5 PeV. The reconstructed shower core is indicated by an asterisk.

Most of the MWPC chambers cover a large surface of about 9 m² and the projective wire and strip read-out entail individual track reconstruction to saturate at particle densities of about 2.0/m². To reduce the ambiguities at higher densities, especially near the shower axis, a third layer of chambers with pad read-out has been installed below the MWPCs. For this purpose limited streamer tubes have been chosen. Their arrangement in six rows and 15 modules each is sketched in Figure 15. The chambers are of the same type and construction style as the chambers of the muon tracking detector which are described in chapter 5 below. As chamber gas pure CO₂ is used for safety reasons because the basement of the central detector has to be accessible to personnel. For this gas the streamers are less well defined locally, but in case of a pad read-out this is of minor relevance. The pad structure is realized on the upper cathode for a module of six tubes with a rectangular size of 8.2 × 16.2 cm². The anode wires are read out as well, but are electronically connected together in pairs. As an example of muon detection in the in-

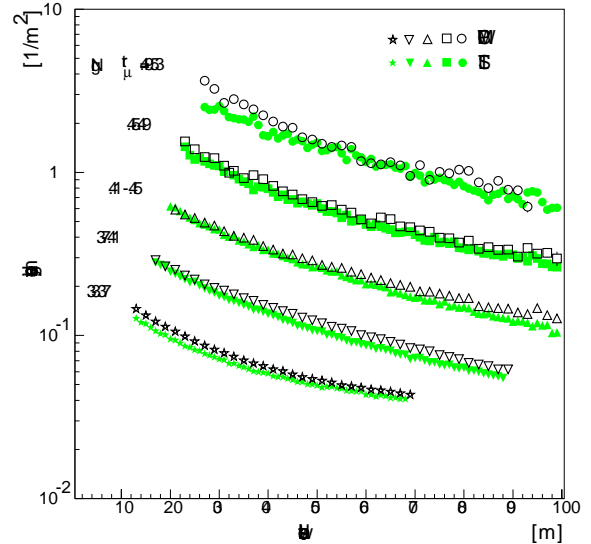


Fig. 22. Muon lateral density distributions for five shower sizes and zenith angles $0^{\circ} < \theta < 18^{\circ}$. Open symbols represent muons tracked by the MWPC, filled symbols represent hits in the streamer tube pads, corrected for non-muon hits according to CORSIKA/CRES simulations.

ner part of an EAS the reconstructed hits are presented in Figure 21. The primary of the EAS had an energy of about 2.5 PeV. The shower centre as reconstructed by the e/γ detectors is marked on the graph. One observes that the layer of limited streamer tubes can manage such muon densities well.

Figure 22 shows muon lateral distributions obtained with the two detection systems for comparison: Firstly, with the MWPCs by track reconstruction and secondly, in the limited streamer tubes by hit detection. The latter have been corrected for non-muon hits using CORSIKA/CRES simulations. One can state that both detector systems yield comparable densities and prove that muon detection below the absorber shielding works as well by track as by hit detection. The discrepancies at high densities for the largest muon numbers are currently under investigation.

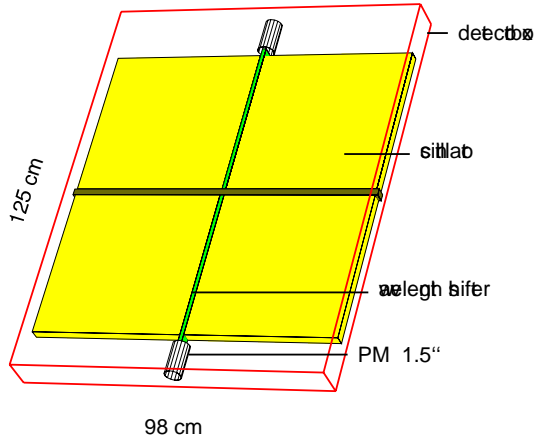


Fig. 23. Sketch of a detector box with two scintillation counters of the trigger layer and top cluster.

4.3 Trigger layer

The layer of scintillation detectors in the third gap is used for fast trigger purposes and for reconstruction of arrival time distributions [14]. A description of the system can be found in [15]. The 456 scintillators cover $2/3$ of the calorimeter area. The absorber thickness above corresponds to $30 X_0$ and efficiently shields the scintillators against the electromagnetic component. For vertical muons the absorber corresponds to a threshold of 490 MeV. Each detector consists of two slabs of a 3 cm thick scintillators of type NE 114, for a sketch see Figure 23. The light is coupled out by a central wavelength shifter bar (type NE 174 A) and measured by a single photomultiplier type EMI 9902. The area of one module is 0.45 m^2 . The most probable energy deposit of passing muons is taken for energy calibration, and calculated to amount to 6.4 MeV. Local variations of light transfer have been determined to be maximal $\pm 4.5\%$. They are small with respect to the Landau fluctuations and sufficient for trigger purposes. The signal threshold is set to $1/3$ of the most probable energy deposit,

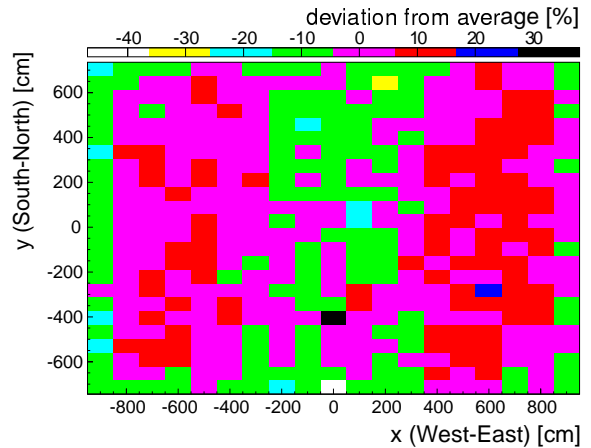


Fig. 24. Homogeneity of the trigger layer for a particular run of 12 h. Shown are the deviations from the average number of hits above threshold for each scintillator.

i.e. to 2.1 MeV. Two kinds of trigger are generated: A multiplicity trigger, if at least eight detectors out of the 456 have a signal above threshold. Figure 24 shows the homogeneity of response for a series of such triggers. A hadron trigger is generated, if in at least one detector a signal of 50 equivalent muons is recorded.

For all scintillation detectors the mean timing resolution has been measured to $\sigma = 1.7 \text{ ns}$ [14]. The individual time delay of each counter was determined using passing muons with respect to a reference counter telescope positioned below the trigger plane in the basement. The stability of this timing has been checked in the beginning by means of light flashes using a system of LEDs, each photomultiplier having its individual light diode. But it turned out that fitting the plane of arrival times in air showers yields equally reliable results and is presently used for the stability check. The time slewing in case of high energetic deposits especially by hadrons is properly taken into account in the analysis of arrival time distributions.

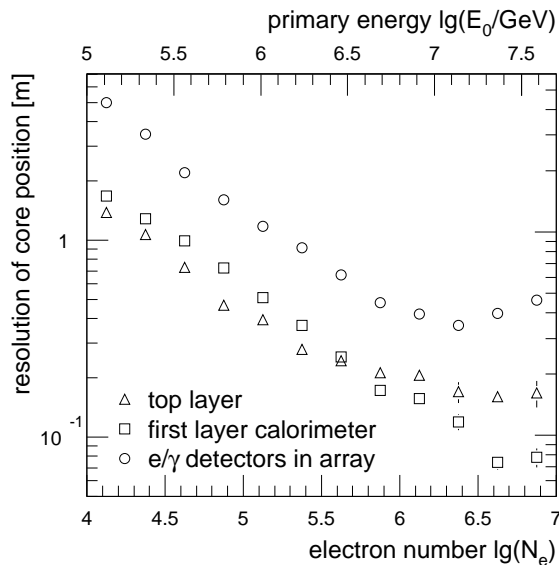


Fig. 25. Resolution for the reconstruction of the core position vs. electron number (lower scale). The primary energy is indicated by the upper scale. Central, proton initiated showers, generated by CORSIKA/CRES are shown ($0^\circ - 30^\circ$ zenith angle).

4.4 Top cluster and top layer

On top of the central detector 25 scintillation counters of the type used in the trigger layer are installed forming the top cluster, see Figure 15. They cover 7.5% of the area and serve, among others, as trigger source for small EAS, e.g. for primary protons below 0.4 PeV. They also fill the gaps of the central four missing array stations.

Directly below the top cluster, a layer of liquid ionization chambers with full surface coverage has come into operation. These chambers are filled with TMP. They have twice the active thickness of liquid as compared to the calorimeter chambers in order to well separate minimum ionizing particles from noise. The most probable energy loss of a muon (1.5 MeV) amounts to more than two times the electronic noise, thus single particles are well recognizable

within a $25 \times 25 \text{ cm}^2$ surface. With this layer the shower centre can be determined as shown in Figure 25. Plotted are the resolutions obtained with three detector systems of KASCADE. If the shower core hits the central detector, the core can be determined precisely by the electromagnetic punch-through to the first active layer of ionization chambers in case of large EAS or by the top layer for small EAS. This allows, to study EAS cores in very detail.

5 Muon tracking detector

North of the central detector the muon tracking detector represents a second device for muon measurements by tracking. It came into operation recently. Figure 26 shows a side view of the installation. A large spacing of 82 cm between three horizontal planes of limited streamer tubes ensures a precise determination of the muon angle and allows to extrapolate the track back to find its production height by means of triangulation. The total length of the detector extends to 32 m and provides an effective detection area of 128 m^2 for vertical particles. The three horizontal layers are supplemented on the sides by vertical chambers in order to accept also inclined tracks, increasing the acceptance to about $500 \text{ m}^2 \text{ sr}$. As counting gas a mixture of 20% argon, 60% isobutane, and 20% CO_2 has proven to give a hit detection of 85%, which results in a three-hit track efficiency of 60%. Investigations to improve the efficiency are currently under way. A detailed description of the muon tracking detector can be found in [16] and of the chamber read-out electronics in [17].

The shielding of concrete, iron, and soil corresponds in vertical direction to $18X_0$ and

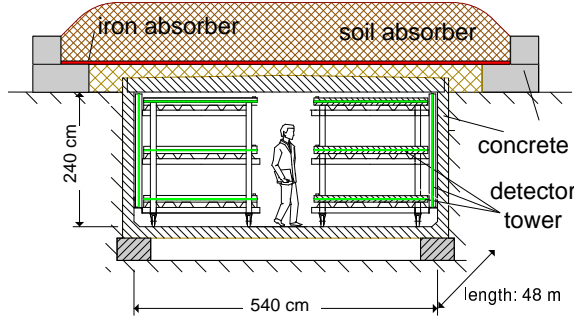


Fig. 26. Sketch of the muon tracking detector with three horizontal and one vertical layer of limited streamer tubes.

entails a muon threshold of 0.8 GeV. The chamber signals are read out at the anode wires with a spacing of 10 mm and at the cathode strips with a pitch of 20 mm. The spatial resolution translates to a geometrical angular precision for vertical tracks of about 0.35° . However, due to interactions of the muons in the shielding and the chamber construction material and because of a finite accuracy in positioning the detectors the full intrinsic resolution has been determined by GEANT simulation to be 0.56° .

Lateral distributions for three muon shower sizes are given in Figure 27 and are compared with the corresponding measurements in the array. The different muon detection threshold has been corrected for by using CORSIKA/CRES simulations. The three muon numbers correspond approximately to 0.3, 0.7, and 1.7 PeV primary energy. One observes that the different detection techniques within KASCADE yield equivalent results.

When extrapolating muon tracks back to find the muon production height, only energetic muons are valuable in order to suppress multiple scattering in the atmosphere and to retain the meson direction in the decay as well as possible. As an indication of a high muon momentum (i.e. above a few GeV), muons with small tangential angles

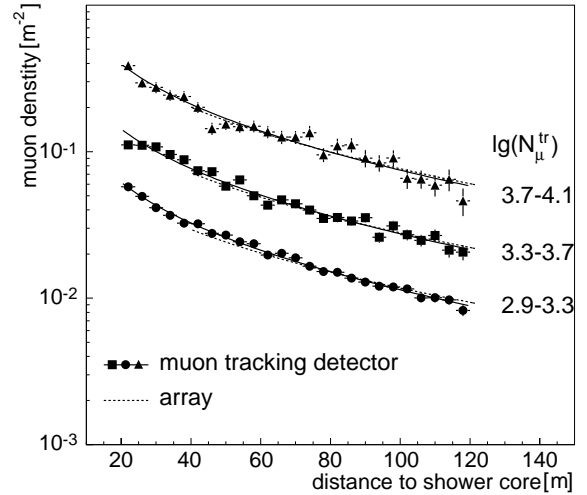


Fig. 27. Muon lateral density distributions for three shower sizes and zenith angles $0^\circ < \theta < 18^\circ$. Symbols represent data from the muon tracking detector. The solid lines are fits to the data, which are corrected for the difference in muon thresholds with respect to the array. The dashed lines are fits to the data of the array for the same shower sample.

are selected. The tangential angle measures the transverse displacement of the muon direction with respect to the shower axis as reconstructed by the e/γ detectors in the array.

Experimentally determined widths of tangential angle distributions are plotted in Figure 28 versus the electron shower size N_e . The average amount of scattering in the atmosphere has been determined by simulations and amounts approximately to 0.2° . This contribution has been subtracted and results in the filled circles. One observes that typical rms-values are between 0.3° and 0.4° . Thus, by limiting the absolute value of the tangential angle to less than 0.7° an effective enrichment of high energy muons is possible. Simulations show that in such samples 75% of the muons have a momentum above 5 GeV. For such muons Figure 29 displays the radial angle distributions for different intervals of muon num-

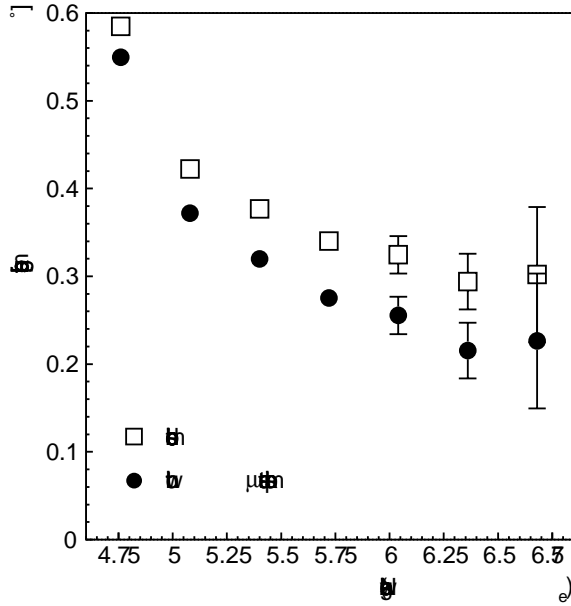


Fig. 28. Rms-values of tangential angle distributions versus electron number N_e . Open symbols represent measured values, from which the multiple muon scattering in the atmosphere is subtracted (filled circles).

bers. As can be inferred from the figure, with increasing muon sizes N_μ^{tr} the radial angles increase and the maxima of the distributions shift to larger values. This reflects the deeper penetration of high-energy showers into the atmosphere.

6 Central Data Acquisition

The detector array, the FADC system, the muon tracking detector, the top-cluster, the trigger plane, the MWPCs and LSTs in the central detector basement as well as the hadron calorimeter are independent experimental components, which can be started, run, read out and stopped alone or together. To correlate the data from different parts of KASCADE, common clock signals are used as outlined in section 3.4.

Figure 30 gives an overview on the basic

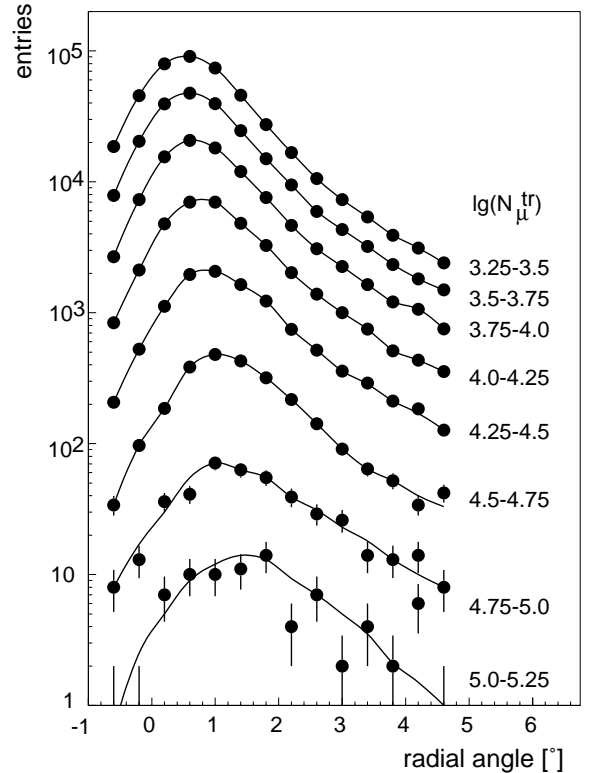


Fig. 29. Frequency distribution of measured radial angles for indicated intervals of N_μ^{tr} and tangential angle $< 0.7^\circ$. The core distances are 40 - 100 m. The lines are drawn to guide the eye.

components of the data acquisition and control system. The system is based on transputers of different types (INMOS T8 and T4) which serve as crate controllers and connecting elements in link interface modules. Altogether the distributed system of transputers forms a parallel computer for each experimental component. They are connected via transputer ether-link gateways (B300) or an alpha processor based VME controller (VME α) to the central workstation. Only the limited streamer tubes and the FADCs do not use transputers. Their VME crates are connected via VME-PCI interfaces in PCs to the central data acquisition.

In case of a trigger, the event data, including the time labels, are transferred from

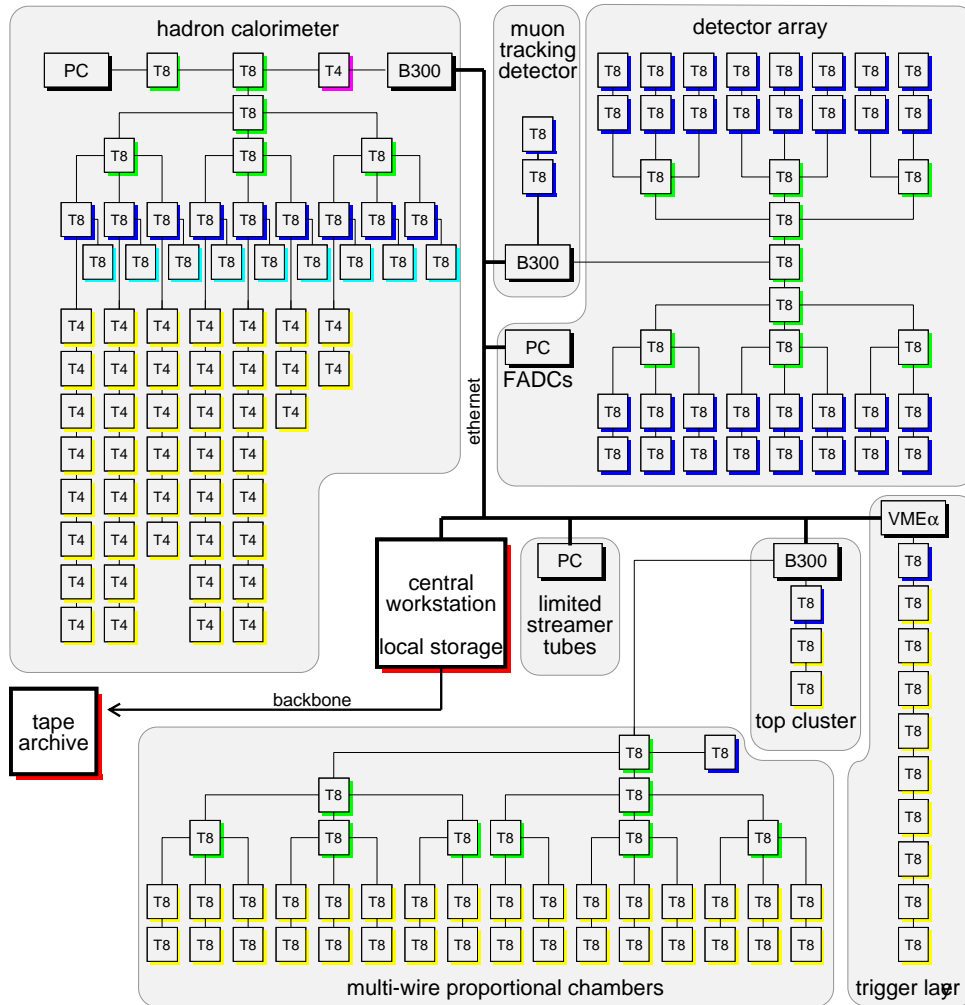


Fig. 30. KASCADE data acquisition system. The system is based on a network of individual processors (transputers), forming a parallel computer for each individual experimental component. The components are connected via ethernet to a central workstation.

the local processor networks of the individual components to the central workstation. There, the main task of the eventbuilder software is the on-line data merging before saving the events on a mass storage device. Data blocks with time differences of less than $6 \mu\text{s}$ around the trigger time are regarded as belonging to the same event. The incoming data blocks are stored in linked lists arranged by arrival times and sorted by their origins.

A large number of other on-line tasks like detector control and calibration, track re-

construction etc. is performed on the local processors. An event display is handled on the central workstation.

The different trigger sources in the experiment are used to study a broad variety of physics problems.

The main trigger source for the study of the primary spectrum and the composition around the knee is a cluster detector multiplicity, fulfilled in at least one array cluster. Typical trigger requirements are $n_o = 10$ to 15 , $n_i = 20$ to 30 , correspond-

ing to rates of 3 to 1 s^{-1} . The resulting threshold of the measurements is a few times 10^{14} eV, depending on zenith angle and primary mass, see Figure 12. The upper limit of the energy range of the experiment is defined by the size of the detector array. About 2 events/day above 10^{17} eV are measured and reconstructed. In most cases the array trigger is accompanied by a muon multiplicity trigger from the trigger layer in the central detector. A local high energy deposit in one station of the detector array can be used as additional trigger condition to study very narrow events.

The single hadron trigger of the central detector trigger layer with a rate of about 0.5 s^{-1} is used to study the flux spectrum of unaccompanied high-energy hadrons. The top cluster and the array detectors are used to select clean single hadron events. The simulations indicate that these events allow to study primary protons in the energy range from 0.5 TeV up to 100 TeV.

The multiplicity trigger of the top cluster (10 out of 50) is used to read out the whole experiment in the case of low energy central shower events. This enables a detailed and complete study of all components of showers with energies larger than typically $5 \cdot 10^{13}$ eV. In this energy range the predictions from EAS simulation codes like CORSIKA can be tested most efficiently by comparing results with direct cosmic ray measurements. The number and distribution of muons and hadrons in the cores of these showers can be determined with good accuracy.

The muon tracking detector can produce its own muon multiplicity trigger, but normally its read-out is triggered from the array clusters or the central detector system.

7 Conclusion and Outlook

Since 1996 the experiment has taken data continuously, in total $8 \cdot 10^8$ showers up to the end of 2002. A host of interesting results has been obtained, e.g. on the knee structure in the energy spectrum, the primary mass composition and the hadronic interaction in the forward direction. The analysis procedures have improved considerably, not least due to redundant data which allow important consistency checks. Regular calibrations and cross calibrations, tests of efficiency and uniformity in response proved to be essential to retain stability and reliability.

Actually, the KASCADE-Grande array [18] starts operation as a joint application of the KASCADE experiment and the EAS-TOP array detectors [19]. They cover a surface of 0.5 km^2 and will allow to extend the measurements up to 10^{18} eV. The scientific goal is to establish the anticipated *knee* of the iron group and to test hadronic interaction models which have to be applied at even higher energies.

Acknowledgments

The authors would like to thank the members of the engineering and technical staff of the collaboration who contributed with enthusiasm and engagement to the success of the experiment. The KASCADE experiment is supported by the German Federal Ministry of Education and Research. Additional support has been provided by collaborative WtZ projects between Germany and Romania (RUM 97/014), Poland (POL 99/005), and Armenia (ARM 02/98). The Polish group acknowledges the

support by KBN grant no. 5PO3B 13320.

References

- [1] P. Doll et al., "The Karlsruhe cosmic-ray project KASCADE", report KfK 4686, Kernforschungszentrum Karlsruhe, 1990.
- [2] D. Heck et al., "CORSIKA: A Monte Carlo code to simulate extensive air showers", report FZKA 6019, Forschungszentrum Karlsruhe, 1998; and www-ik.fzk.de/~heck/corsika/
- [3] GEANT: CERN report DD/EE/84/1 (1987).
- [4] G. Völker, "A detector system for the measurement of the electromagnetic component of EAS at ultra high energies", report KfK 4983, Kernforschungszentrum Karlsruhe, 1992, in German.
- [5] W. Kriegleder, "A detector system for the measurement of muons in extensive air showers", report KfK 5023, Kernforschungszentrum Karlsruhe, 1992, in German.
- [6] H. Schieler, "Development and test of the local data acquisition system for the structured detector array of the KASCADE experiment", Doctoral thesis, University of Karlsruhe, 1996, in German.
- [7] J. Zabierowski et al., Nucl. Instr. and Meth. A 354 (1995) 496.
- [8] T. Antoni et al., Astrop. Phys. 14 (2001) 245.
- [9] H.J. Mayer, Nucl. Instr. and Meth. A317 (1992) 339.
- [10] H.J. Mayer, Nucl. Instr. and Meth. A330 (1993) 254.
- [11] J. Engler et al., Nucl. Instr. and Meth. A427 (1999) 528.
- [12] T. Antoni et al., J. Phys. G: Nucl. Part. Phys. 25 (1999) 2161.
- [13] H. Bozdog et al., Nucl. Instr. and Meth. A465 (2001) 455.
- [14] T. Antoni et al., Astropart. Phys. 15 (2001) 149.
- [15] M. Brendle and U. Raidt, Nucl. Instr. and Meth. A 412 (1998) 420; U. Raidt, "Set-up of a trigger and timing facility for the KASCADE central detector", report FZKA 5917, Forschungszentrum Karlsruhe 1997, in German.
- [16] P. Doll et al., Nucl. Instr. and Meth. A488 (2002) 517.
- [17] J. Zabierowski and P. Doll, Nucl. Instr. and Meth. A484 (2002) 528.
- [18] M. Bertaina et al., Proc. 27th Int. Cosmic Ray Conf., Hamburg 2 (2001) 792; K.-H. Kampert et al., Nucl. Phys. B (Proc. Suppl.) 2003 in press; and astro-ph/0212347.
- [19] M. Aglietta et al., Nucl. Instr. and Meth. A 277 (1989) 23